Compressive Millimeter-Wave Phased Array Imaging

Qiao Cheng, *Student Member, IEEE,* Akram Alomainy, *Senior Member, IEEE,* and Yang Hao, *Fellow, IEEE*

***Abstract*—In this paper, we introduce a three-dimensional (3-D) compressive phased array imaging method. The derived system model is general and can also be used in other array configurations. With its compressive sampling capability, the proposed method can recover images with far fewer samples than traditionally required in Fourier transform (FT) based methods. This measurement strategy greatly reduces the data acquisition time at the expense of higher computational costs. Imaging results show increased resolving power in both range and cross-range directions. Moreover, the use of beam steered data enables better reconstruction quality in the presence of noise than its counterpart in switched array scheme. Sensing configurations like array length and number of angles, which affect the reconstruction performance, are also analyzed.**

***Index Terms*—Phased array, beamforming, antenna array, three-dimensional imaging, compressive sensing.**

I. Introduction

Microwave and millimeter-wave (MMW) imaging systems are of great interest in many applications such as nondestructive testing and evaluation (NDT&E), security scanning, medical diagnosis and through-wall imaging [1]–[5]. Traditional aperture antennas used in MMW imaging systems like reflectors and lenses offer low-cost hardware and compact design but suffer from relatively low resolution and slow mechanical scanning. On the other hand, antenna array solutions provide electronic flexibility in exciting the elements, allowing for faster scanning in real time applications.

There are already many array configurations that have been proposed for imaging applications in the open literature and in some cases commercially deployed. The simplest one is to sequentially switch on and off the array elements, e.g., [2] combined linear switched array with synthetic aperture radar (SAR) concept and designed a MMW concealed weapon detection system that can accomplish data acquisition in nearly 1 second. The disadvantage of the switched array scheme is its low efficiency, as all elements work separately. Recently, multiple-input multiple-output (MIMO) array imaging has attracted significant attention [6], [7]. The essence of the MIMO array concept is to employ multiple transmitters and multiple receivers sequentially or simultaneously [8]. The increased spatial diversity of MIMO configuration enables sparse array design while preserving high resolution image reconstruction. The switched array and MIMO array are also known as monostatic array and multistatic array systems, respectively. More recently, digital beamforming receiver array concept was introduced to MIMO array to maximize the signal-to-noise ratio (SNR) of the imaging system [9]. SNR is a critical parameter in radar system which essentially describes the difference between the desired signal and the unwanted noise. Comparing to the conventional hardware phased array which employs beamforming in both transmit and receive modes, digital beamforming receiver array has lower gain but is easier to implement and can dramatically reduce the system cost.

In order to form three-dimensional (3-D) images, two-dimensional (2-D) array with wideband signals are often required [2]. However, the standard Fourier transform (FT) based image reconstruction methods [7], [10] require a substantial amount of data to be uniformly sampled during data acquisition. As the reconstructed 3-D image is a map of the spatial distribution of the reflectivity function of stationary targets, the reconstruction can be sparse or compressible in some representation. Therefore, this issue can be alleviated by using the recently introduced theory of compressive sensing (CS) [11], [12]. CS theory guarantees signal reconstruction from highly undersampled data provided that the signal is sparse and proper sensing matrix is adopted. By utilizing the sparse nature of the target scene, CS enables efficient sampling to speed up the data acquisition process of an imaging system. The CS technique has been successfully applied to many imaging applications including (but not limited to) MMW holography [13]–[15], SAR imaging [16]–[19] and inverse scattering [20], [21]. Particularly, in [14], a 2-D switched array MMW holography imaging method was proposed by combining FT based forward and backward operators with the CS framework. The performance of this method, together with the direct CS (D-CS) method, have been thoroughly studied in [15]. Results indicated that the D-CS method achieves better resolution than the FT-CS method but requires higher computing power. The MIMO array case has been discussed in [22] in the context of SAR imaging. A new mutual coherence metric was proposed and verified to be effective in examining the reconstruction quality of various array configurations.

In this paper, a general forward model is derived for array based imaging systems by taking into consideration the antenna factors such that it can be easily applied to different array configurations with slight modifications. Thereafter, we introduce a 3-D compressive imaging method for phased array systems. To the best of the authors' knowledge, this paper for the first time introduces the CS theory to 2-D phased arrays for 3-D imaging. This method does not require interpolation and gives accurate reconstruction of the target's true reflectivity. Comparing to conventional FT methods, the proposed

Manuscript received Nov xx, 2016. This work was supported by the EPSRC Grant EP/I034548/1 and the China Scholarship Council (CSC).

The authors are with the School of Electronic Engineering and Computer Science, Queen Mary, University of London, London E1 4NS, UK (e-mail: q.cheng@qmul.ac.uk).

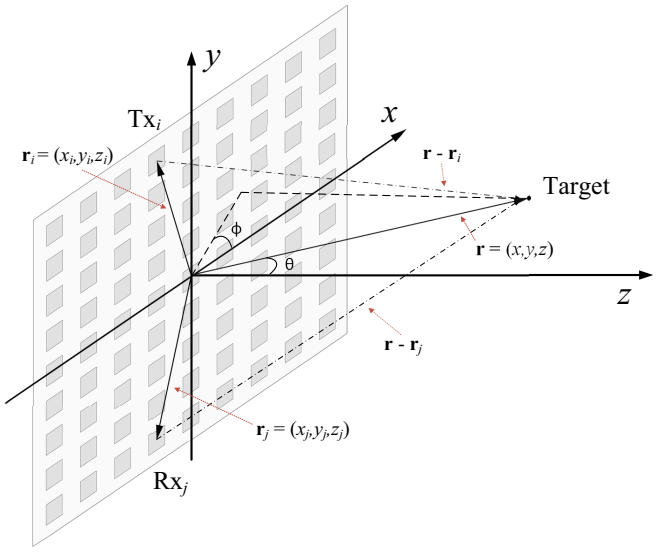

Fig. 1. Three-dimensional imaging using 2-D phased array and wideband signals. By assigning appropriate weights to each element, the main beam of the array is focused in the direction of (θ, ϕ) while the sidelobes are suppressed in the undesired directions.

approach achieves significantly higher image resolution and is more robust to noise even with only a small number of random measurements. We also provide an analysis on how to design the sensing configuration for better CS reconstruction results.

The remainder of this paper is organized as follows. Section II presents the forward model for array based imaging systems. In section III, we present the 3-D compressive phased array imaging method and discuss the reconstruction algorithms. Section IV evaluates the performance of the proposed method with both 3-D and 2-D data. Finally, section V summarizes the results and concludes this paper.

II. Phased Array Imaging Forward Model

The 3-D imaging model shown in Fig.1 is interpreted in the dimension of range and cross-range. The range (z) is the direction of wave propagation and the cross-range (x or y) is the direction parallel to the array aperture. A 2-D planar array is located in the x-y plane with its center in the origin. All elements are evenly spaced in both x and y dimensions. The amplitude and phase of the elements across the array are adjusted so that the main beam of the radiation pattern is directed towards a specified direction. By continuously illuminating the target region with directional beams of different elevation angle θ and azimuth angle ϕ, where $\theta \in [0, \pi/2]$ and $\phi \in [0, 2\pi)$, the reflectivity information of the target region can be reconstructed from the reflected data.

Assuming an observing point $\mathbf{r} = (x, y, z)$ is at the far field of an antenna element, the electric field radiated from the i-th antenna at $\mathbf{r}_i = (x_i, y_i, z_i)$ can be written as [23]

$$\mathbf{E}_i(\mathbf{r}, k) = P_i(\mathbf{r}) \frac{\exp(-jk|\mathbf{r} - \mathbf{r}_i|)}{|\mathbf{r} - \mathbf{r}_i|}, \tag{1}$$

where $P_i(\mathbf{r})$ is the element pattern, $k = 2\pi f/c$ is the wavenumber at frequency f and $|\mathbf{r} - \mathbf{r}_i| = \sqrt{(x - x_i)^2 + (y - y_i)^2 + (z - z_i)^2}$ is the distance between $\mathbf{r}$ and $\mathbf{r}_i$. In general, it is assumed that all element patterns are the same. Assuming the mutual coupling effects among elements can be neglected, the total transmitted electric field can be calculated by the superposition of all elements

$$\mathbf{E}_\mathbf{T}(\mathbf{r}, k) = P(\mathbf{r}) \sum_i W_i \frac{\exp(-jk|\mathbf{r} - \mathbf{r}_i|)}{|\mathbf{r} - \mathbf{r}_i|}. \tag{2}$$

The coefficient $W_i = |W_i| \exp(-j\Psi_i)$ is the complex weight with amplitude $|W_i|$ and phase Ψ_i added to the ith element. In order to steer the antenna beam in a certain direction, e.g., (θ, ϕ), the phase term has to be in the form of [23]

$$\Psi_i = k\hat{\mathbf{r}}_0 \cdot \mathbf{r}_i, \tag{3}$$

where $\hat{\mathbf{r}}_0 = \hat{\mathbf{x}} \sin\theta \cos\phi + \hat{\mathbf{y}} \sin\theta \sin\phi + \hat{\mathbf{z}} \cos\theta$ is the unit vector in the direction of (θ, ϕ). By substituting (3) into (2) and neglecting the amplitude term, we get the total field when beam is steered towards (θ, ϕ)

$$\mathbf{E}_\mathbf{T}(\mathbf{r}, k, \theta, \phi) = P(\mathbf{r}) \sum_i \frac{\exp[-jk(\hat{\mathbf{r}}_0 \cdot \mathbf{r}_i + |\mathbf{r} - \mathbf{r}_i|)]}{|\mathbf{r} - \mathbf{r}_i|}. \tag{4}$$

According to the reciprocity theorem, the transmit and receive properties of an antenna are identical. Therefore, each element in the phased array shares the same pattern and phase delay in both transmitting and receiving models. Assuming there is a point scatterer at the observing point $\mathbf{r} = (x, y, z)$ with frequency independent reflectivity $g(\mathbf{r})$. The reflected electric field received by the j-th antenna at $\mathbf{r}_j = (x_j, y_j, z_j)$ can be denoted as

$$\mathbf{E}_j(\mathbf{r}, k, \theta, \phi) = P(\mathbf{r}) g(\mathbf{r}) \mathbf{E}_\mathbf{T}(\mathbf{r}, k, \theta, \phi) \times \frac{\exp[-jk(\hat{\mathbf{r}}_0 \cdot \mathbf{r}_j + |\mathbf{r} - \mathbf{r}_j|)]}{|\mathbf{r} - \mathbf{r}_j|}. \tag{5}$$

Similarly, by summing the electric field of all receiving elements and combining (4), the total received field of the phased array due to a point scatterer at $\mathbf{r}$ can be written as

$$\mathbf{E}_\mathbf{R}(\mathbf{r}, k, \theta, \phi) = P(\mathbf{r})^2 g(\mathbf{r}) \sum_i \sum_j \times \frac{\exp[-jk(\hat{\mathbf{r}}_0 \cdot \mathbf{r}_i + |\mathbf{r} - \mathbf{r}_i| + \hat{\mathbf{r}}_0 \cdot \mathbf{r}_j + |\mathbf{r} - \mathbf{r}_j|)]}{|\mathbf{r} - \mathbf{r}_i||\mathbf{r} - \mathbf{r}_j|}. \tag{6}$$

Under the assumption of Born approximation, i.e., neglecting any mutual interaction between the targets, the total reflected field from all scatterers can be expressed as

$$s(k, \theta, \phi) = \iiint_V \mathbf{E}_\mathbf{R}(\mathbf{r}, k, \theta, \phi)\, dx\, dy\, dz, \tag{7}$$

where V represents the 3-D target region.

It is worth noting that although we assume using transceiver module based array, the above forward model is also applicable to other phased array configurations, e.g., digital beamforming receiver array case can just ignore the transmitter beamforming in (2). Moreover, by assigning random complex weight W_i to each antenna, the forward model can be used for arrays with arbitrary radiation patterns. Since the far field assumption in (1) is based on a single antenna and the near

field region of an array is usually much farther than it is of a single antenna, the forward model is still effective in the near field region of an array.

The term $P(\mathbf{r})$ in (6), which is also called the element factor, plays an important role in the beamforming performance. In the case of using isotropic antenna which has the same intensity of radiation in all directions, the $P(\mathbf{r})$ term can be dropped in the above equations. By doing so and rewriting the vectors as in the cartesian coordinates, (6) becomes identical to those in [10] (2-D in range and cross-range) and [24] (2-D in cross-range). Without loss of generality, we also adopt this isotropic antenna assumption in the following discussions.

The forward model in (7) describes how electromagnetic waves interact with targets. Our goal is to reconstruct the reflectivity function $g(\mathbf{r})$ from the received data. To avoid missing vital information, the angles ϕ and θ should be chosen to cover the complete target region. The sampling intervals in both angle and frequency domains should follow the Nyquist theorem to avoid aliasing. In conventional FT inversion techniques [10], [24], the term $\exp(-jk|\mathbf{r}-\mathbf{r}_i|)/|\mathbf{r}-\mathbf{r}_i|$ and $\exp(-jk|\mathbf{r}-\mathbf{r}_j|)/|\mathbf{r}-\mathbf{r}_j|$ are first decomposed into integrals over wavenumber domain and then processed with inverse FT algorithms. As the inverse FT requires uniformly spaced data in (k_x, k_y, k_z) domain, the received data which is uniformly spaced in (k, θ, ϕ) domain needs to be interpolated according to dispersion relations. There are drawbacks in this process. Firstly, by utilizing the Fourier decomposition, the FT method is actually trying to solve an approximated model of (7). In other words, the FT solution is only an approximation to the true reflectivity. Secondly, the accuracy of interpolation from (k, θ, ϕ) domain to (k_x, k_y, k_z) domain is highly dependent on the choice of interpolation techniques. Owing to the approximation nature of interpolation, the inaccuracy of this process cannot be avoided. In the next section, we will show the proposed CS method can overcome both issues.

III. Compressive Sensing Implementation

A. CS Forward Model

We first rewrite the vectors in (7) into coordinates form. Suppose $N_{tx} \times N_{ty}$ is the number of antennas in the transmitting aperture and $N_{rx} \times N_{ry}$ is the number of antennas in the receiving aperture. As the array is 2-D, we denote by $(a(i), b(j))$ the x-y coordinates of the (i,j)-th element in the transmitting array and $(u(i), v(j))$ the x-y coordinates of the (i,j)-th element in the receiving array. Thus, (7) can be rewritten as

$$\begin{aligned} s(k,\theta,\phi) = \iiint_V & \sum_{m_1=1}^{N_{tx}} \sum_{m_2=1}^{N_{ty}} \sum_{n_1=1}^{N_{rx}} \sum_{n_2=1}^{N_{ry}} g(x,y,z) \\ & \times C(a(m_1), b(m_2), x, y, z, k) C(u(n_1), v(n_2), x, y, z, k) \\ & \times \exp[-j(\Psi(a(m_1), b(m_2), k, \theta, \phi) \\ & + \Psi(u(m_1), v(m_2), k, \theta, \phi))]\, dx\, dy\, dz, \end{aligned} \quad (8)$$

where

$$C(x_0, y_0, x, y, z, k) = \frac{\exp(-jk\sqrt{(x-x_0)^2+(y-y_0)^2+(z-0)^2})}{\sqrt{(x-x_0)^2+(y-y_0)^2+(z-0)^2}} \quad (9)$$

and

$$\Psi(x_0, y_0, k, \theta, \phi) = k(x_0 \sin\theta\cos\phi + y_0 \sin\theta \sin\phi). \quad (10)$$

In order to apply CS algorithms, the target region needs to be discretized and (8) should be reformulated into the following matrix multiplication form

$$\mathbf{s} = \mathbf{H}\mathbf{g}, \quad (11)$$

where $\mathbf{s}$ and $\mathbf{g}$ are the vector versions of $s(k,\theta,\phi)$ and $g(x,y,z)$, respectively. $\mathbf{H}$ is the system response matrix and can be treated as a dictionary matrix from the perspective of CS theory. More specifically, suppose the 3-D target region V can be discretized into $P \times Q \times R$ voxels and we denote by I, J and K the number of frequency points, azimuth angles and elevation angles used during data acquisition. Then (11) can be rewritten as

$$\begin{bmatrix} \mathbf{s}(1) \\ \vdots \\ \mathbf{s}(IJK) \end{bmatrix} = \begin{bmatrix} \mathbf{H}_{1,1} & \cdots & \mathbf{H}_{1,PQR} \\ \vdots & \ddots & \vdots \\ \mathbf{H}_{IJK,1} & \cdots & \mathbf{H}_{IJK,PQR} \end{bmatrix} \begin{bmatrix} \mathbf{g}(1) \\ \vdots \\ \mathbf{g}(PQR) \end{bmatrix}, \quad (12)$$

where element $\mathbf{H}_{i,j}$ is determined by the summation in (8) with certain k, θ, ϕ and voxel coordinates. Specifically, the i-th column of $\mathbf{H}$ is related to the coordinates of the i-th voxel in $\mathbf{g}$. Each row of $\mathbf{H}$ is related to specific values of k, θ and ϕ. These parameters are of vital importance in determining the quality of CS reconstruction, which will be discussed in the next section.

B. CS Reconstruction

In conventional FT methods, the sampling intervals have to satisfy the Nyquist theorem to avoid aliasing. With CS theory, we are able to break this restriction by randomly undersampling in the θ, ϕ and k domains. Mathematically, this is realized by randomly selecting a set of rows in $\mathbf{H}$. Let $\mathbf{y}$ be the undersampled data and $\mathbf{A}$ the row selection matrix, the final CS model can be written as

$$\mathbf{y} = \mathbf{A}\mathbf{H}\mathbf{g}. \quad (13)$$

As (13) is an underdetermined system, it has infinite solutions. CS theory offers an alternative way to solve this by enforcing a sparsity constraint on the solution:

$$\min_{\mathbf{g}} \|\mathbf{g}\|_0 \quad s.t. \;\; \mathbf{y} = \mathbf{A}\mathbf{H}\mathbf{g}, \quad (14)$$

where $\|\mathbf{x}\|_0$ is the number of nonzeros of vector $\mathbf{x}$. Unfortunately, (14) is computationally difficult to solve. A more general approach is to relax the ℓ_0 norm to ℓ_1 norm:

$$\min_{\mathbf{g}} \|\mathbf{g}\|_1 \quad s.t. \;\; \mathbf{y} = \mathbf{A}\mathbf{H}\mathbf{g}, \quad (15)$$

where $\|\mathbf{x}\|_1 = \sum_i |(\mathbf{x}_i)|$ is the ℓ_1 norm of vector $\mathbf{x}$. This minimization problem is often known as Basis Pursuit (BP) [12]. Considering the imaging system is always accompanied with noise, (15) is commonly solved by rewriting it as a Basis Pursuit Denoising (BPDN) [25] problem:

$$\min_{\mathbf{g}} \|\mathbf{g}\|_1 \quad s.t. \quad \|\mathbf{AHg} - \mathbf{y}\|_2^2 \leq \varepsilon, \tag{16}$$

and ε is a nonnegative real parameter that defines the noise level. There are many algorithms available to solve the above ℓ_1 minimization. We adopt the two-step iterative shrinkage-thresholding (TwIST) algorithm which solves the Lagrangian relaxation of (16) with faster convergence rate than traditional algorithms [26]. The final minimization problem can be expressed as:

$$\hat{\mathbf{g}} = \underset{\mathbf{g}}{\operatorname{argmin}} \frac{1}{2} \|\mathbf{AHg} - \mathbf{y}\|_2^2 + \lambda \|\mathbf{g}\|_1, \tag{17}$$

where λ is the regularization parameter which controls the tradeoff between the sparsity of the solution and its closeness to the least squares solution.

The key requirement to ensure the solution to both (14) and (15) will coincide is the sensing matrix $\mathbf{\Phi} = \mathbf{AH}$ has to satisfy the Restricted Isometry Property (RIP) [27]. It has been proven that certain matrices satisfy the RIP with high probability, e.g., random Gaussian and Bernoulli matrices. However, verifying if a deterministic matrix has this property is computationally infeasible. Fortunately, the mutual coherence [28] is an alternative measure of the ability to accurately reconstruct a signal. The mutual coherence of a matrix $\mathbf{\Phi}$, denoted as $\mu(\mathbf{\Phi})$, is the largest absolute normalized inner product between different columns of the matrix:

$$\mu(\mathbf{\Phi}) = \max g_{ij}, \qquad g_{ij} = \frac{\left|\boldsymbol{\phi}_i^T \boldsymbol{\phi}_j\right|}{\|\boldsymbol{\phi}_i\|_2 \cdot \|\boldsymbol{\phi}_j\|_2} (i \neq j), \tag{18}$$

where $\boldsymbol{\phi}_i$ is the ith column of $\mathbf{\Phi}$. This metric was empirically shown to be proportional to mean-squared-error (MSE) values for reconstructions [29]. Generally, a sensing configuration that has lower mutual coherence in $\mathbf{\Phi}$ gives lower MSE in reconstruction. Although simple in formulation, the mutual coherence metric is too conservative in many imaging applications. This is due to the fact that there might be some similar columns in $\mathbf{\Phi}$, which can unfairly dominate the mutual coherence. To address this issue, researchers have proposed average mutual coherence [30], t-average mutual coherence [31] and $t_{\%}$-average mutual coherence [22]. The $t_{\%}$-average mutual coherence is defined as:

$$\mu_{t_{\%}}(\mathbf{\Phi}) = \frac{\sum_{i \neq j} g_{ij} \sigma_{ij}}{\sum_{i \neq j} \sigma_{ij}}, \quad \sigma_{ij} = \begin{cases} 1, & g_{ij} \in \mathcal{E}_{t_{\%}} \\ 0, & \text{otherwise}, \end{cases} \tag{19}$$

where $\mathcal{E}_{\%}$ is the set of $t_{\%}$ percent of the largest column cross-correlations g_{ij}. This metric mitigates the outlier issue and hence is better suited as an indication of the reconstruction performance.

Another key requirement for successful CS reconstruction is the signal sparsity. The sparser the signal is, the fewer measurements needed for reconstruction are. Just as in the classical CS theory, the image sparsity in our case can also be classified into two categories. In the first category, the target region is dominated by few point scatterers, e.g., some SAR imaging applications. ℓ_1 norm as shown in (15) is already enough to exploit the image sparsity. In the second case, the target region is much more complicated and the image scene is no longer sparse in the spatial domain, e.g., security imaging for concealed weapon detection. In such cases, sparsity transforms like total variation (TV) [32] are usually added to promote the image sparsity. It should also be noted that the data format in the above equations is complex-valued. Conventional sparsifying transforms and sparsity constraints for real-valued applications might be less effective for complex data. How to optimally promote the sparsity of the complex-valued data is still an open problem and requires further research.

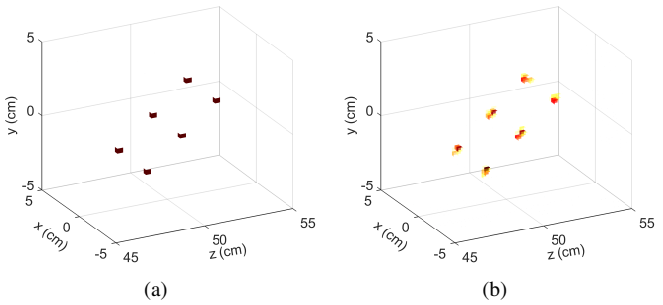

Fig. 2. Three-dimensional reconstruction of 6 point scatterers. (a) Ground truth of the target scene. (b) Reconstruction by the proposed method.

IV. Numerical Investigations and Analysis

To examine the effectiveness of the proposed method, we first demonstrate image reconstruction in 3-D space. The imaging capabilities are then thoroughly studied for 2-D imaging with both qualitative and quantitative results.

A. Imaging of 3-D Scene

The simulation is carried out in the MMW frequency band centered at 60 GHz. We assume 20 GHz bandwidth for better range resolution. The length of the array is 6 cm in both x and y dimensions with element spacing fixed at the half of the wavelength of the highest frequency, that is, 2.1 mm. It is worth noting that half-wavelength spacing may violate the Nyquist sampling requirement, but it is chosen so for two reasons. Firstly, element spacing smaller than half-wavelength can be challenging in engineering realization. Secondly, mutual coupling of antenna elements becomes a big issue with closely spaced elements. The resulting array geometry consists of 29 elements in each dimension and 841 elements in total. Elevation angle and azimuth angle are varied within the interval of $[0°, 8°]$ and $[0, 360°)$, respectively, to cover the target region. During data acquisition, 20 frequency points, 15 azimuth angles and 15 elevation angles, all evenly spaced, are deployed to illuminate the target area.

The 3-D target scene, shown in Fig. 2(a), is 45 cm away from the aperture with dimension of 10 cm×10 cm×10 cm. We consider 6 point scatterers in the target region, each with unit reflectivity. The coordinates of the 6 targets are $(\pm 2, -2, 48)$, $(\pm 2, 0, 50)$ and $(\pm 2, 2, 52)$. Equation (8) is

adopted to calculate the reflected fields in simulation. In CS implementation, for the ease of computation, we discretize the target scene into $41\times41\times41$ voxels. It should be noted that the selected sampling intervals in frequency and angle domain already violate the Nyquist criteria according to [10]. Fig. 2(b) gives the reconstruction result of using only 10% random samples of the undersampled $20\times15\times15$ measurements. As clearly shown, all 6 targets have been correctly reconstructed by the proposed method.

B. Imaging of 2-D scene

Comparing to the 2-D imaging, the 3-D case is computationally more expensive and requires higher memory usage. The construction of the $\mathbf{H}$ matrix can be extremely time-consuming when fine grid spacing is adopted. For these reasons, we concentrate our analysis on the 2-D imaging in cross-range (x) and range (z) dimensions, in a similar fashion to the 2-D SAR imaging. Because the missing y-dimension is the same as the x-dimension, the results in the 2-D case can be easily scaled to the 3-D case with suitable computational powers.

In the 2-D case, the azimuth angle ϕ is fixed at 0° or 180°, hence equation (10) can be simplified to $\Psi(x_0,k,\theta,\phi) = kx_0\sin\theta\cos\phi$. We assume a linear array of length 8 cm (40 elements) is centered at the origin along the x axis. One hundred equally spaced elevation angles are scanned from 0° to 24°. The bandwidth is still 20 GHz but 40 frequency points are used in this case. The reconstructed area is extended to 30cm in both range and cross-range dimensions. A finer discretization of 121×121 pixels is adopted. We consider 9×9 equally spaced point scatterers with an interval of 2.5 cm. Fig. 3(a) and Fig. 3(b) represent the reconstruction results of the FT method [10], [33] with 40% data and 100% data, respectively. Both figures are very blurry and the reconstructed targets are barely identifiable. Moreover, Fig. 3(a) exhibits more noise in the background due to undersampling. In contrast, as shown in Fig. 3(c), the CS method accurately reconstructed all targets and is free from background noise.

Given a sensing configuration, the minimum required number of measurements for accurate reconstruction is determined by the sparsity of the target scene. Generally, the sparser the target scene is, the fewer measurements are required. Fig. 3(d) quantitatively summarizes the reconstruction quality of the proposed method as a function of undersampling rate. Note the MSE is averaged over the results of 50 independent trials for each sampling rate. It can be observed that the curve gradually becomes flat as the sampling rate reaches 30%, which indicates the minimum required number of measurements for this case is around 30% of the full measurements. Increasing the number of measurements after the 30% threshold is a waste of time as no obvious improvement can be observed. In most practical situations, the target scene can be much more complicated. Therefore, it is of great importance to obtain empirically the minimum required number of measurements such that the data acquisition time can be maximally reduced.

The resolution of FT methods is determined by the data coverage in the wavenumber domain [10]. It is of interest to establish whether the CS method has the same limitation.

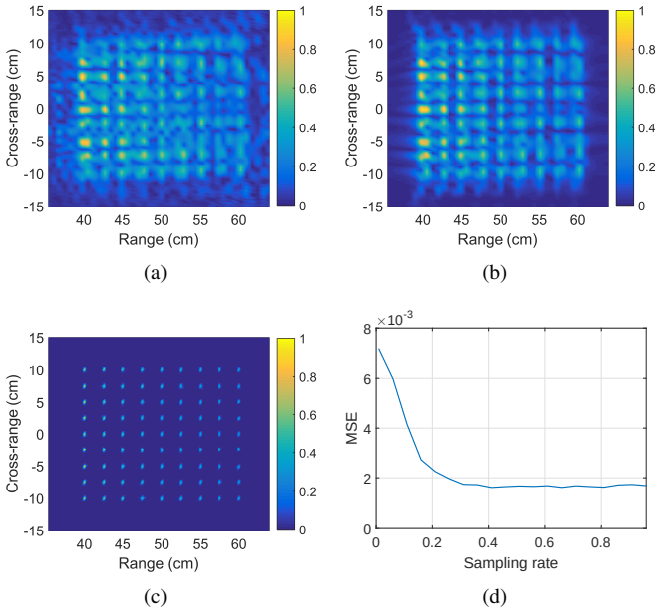

Fig. 3. Reconstruction results of point scatterers by (a) FT method with 40% data, (b) FT method with 100% data and (c) CS method with 40% data. (d) Averaged MSE of the CS method as a function of sampling rate.

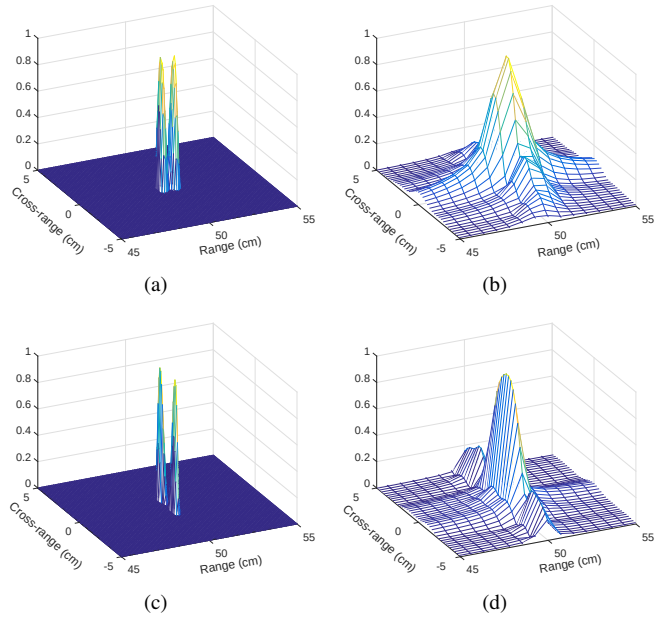

Fig. 4. Two-dimensional reconstruction of double-point scatterers at $(0,0,50\pm0.175)$ and $(0,\pm1,0)$. (a and c) CS method with 10% data. (b and d) FT method with 100% data.

Therefore, we employ several sets of closely spaced double-point scatterers for test. The CS reconstruction based on 10% data is compared to full data reconstruction of the FT method. Reconstructed reflectivity is normalized to $[0,1]$ for the ease of comparison. In the first example, two scatterers with a spacing of 0.35 cm are centered along the range direction. The two targets can be clearly identified in Fig. 4(a) while only one single peak is shown in Fig. 4(b). In a similar manner, the second example compares the reconstructions of

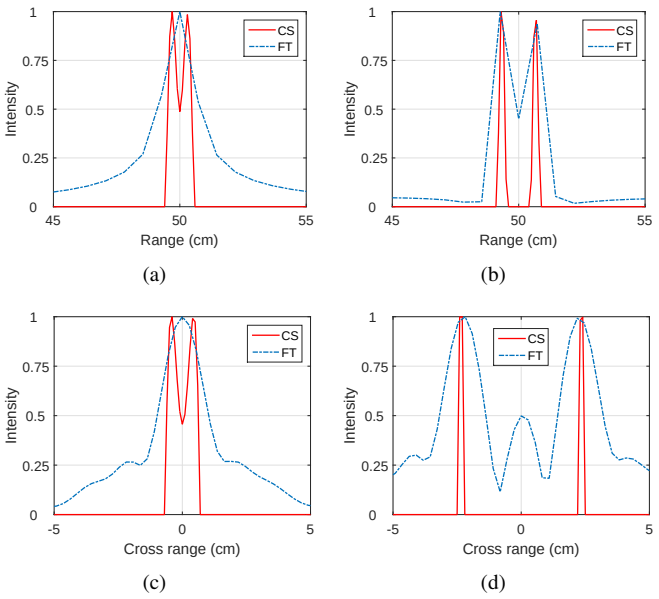

Fig. 5. One-dimensional slice reconstruction of double-point scatterers at (a) $(0, 0, 50 \pm 0.17)$, (b) $(0, 0, 50 \pm 0.65)$, (c) $(0, \pm 0.4, 0)$ and $(0, \pm 2.3, 0)$.

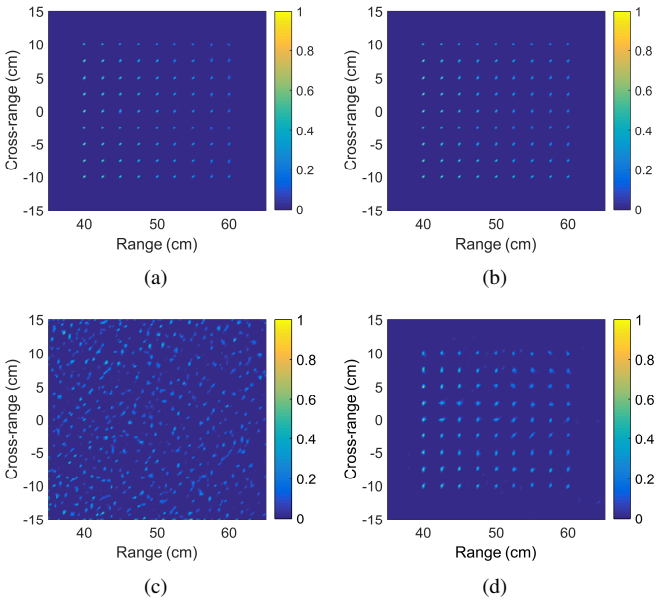

Fig. 6. CS reconstructions of different array configurations using the same number of measurements. (a) Switched array and (b) phased array with 20 dB SNR. (c) Switched array and (d) phased array with -50 dB SNR.

2 cm apart point scatterers in the cross-range direction, as shown in Fig. 4(c) and Fig. 4(d). The CS method again makes the two targets discernible. To better analyze the resolving power of the proposed method, we define the resolution of an imaging system as the distance between two targets when the intersection of the two peaks is at the half power level. Fig. 5(a) and Fig. 5(b) demonstrate the one-dimensional reconstruction intensity of two sets of double-point scatterers located at $(0, 0, 50 \pm 0.17)$ and $(0, 0, 50 \pm 0.65)$, respectively. It can be observed the FT method has a range resolution of 1.3 cm whereas the CS method has improved the resolution to 0.34 cm. Similarly, Fig. 5(c) and Fig. 5(d) show the cross-range direction case where double-point scatterers are located at $(0, \pm 0.4, 0)$ and $(0, \pm 2.3, 0)$. The CS method again has improved the resolution from 4.6 cm to 0.8 cm. Therefore, it can be concluded that the CS method is able to outperform the resolution limit of the FT method in both the range and cross-range directions.

One of the most important advantages of the phased array is the sharpened main beam with suppressed sidelobes. The resulting high gain pattern greatly maximizes the signal-to-noise ratio (SNR) of the imaging systems. To verify this, the imaging results are compared to the results using the switched array scheme in various noise conditions. To do so, we manually add independent and identically distributed (i.i.d.) Gaussian noise to each of the receiving antennas before reconstruction. The two imaging systems share the same array configuration and target scene, i.e., same number of antennas in the same aperture. The main difference is the data acquisition process, that is, the phased array scheme varies the elevation angle while the switched array scheme sequentially switch on and off the linear array (varies antenna locations). It should be noted that both schemes have the same power generation, i.e., the transmitted power of each switched antenna is the same as the total transmitted power of the phased array. The imaging forward model of the switched array scheme is based on [15] by adding the attenuation factor $|\mathbf{r} - \mathbf{r}_i|^2$ as

$$\mathbf{E}(\mathbf{r}_i, k) = \iiint_V g(\mathbf{r}) \frac{\exp(-j2k|\mathbf{r} - \mathbf{r}_i|)}{|\mathbf{r} - \mathbf{r}_i|^2} \, dx \, dy \, dz, \qquad (20)$$

where $\mathbf{E}(\mathbf{r}_i, k)$ stands for the received field at the i-th antenna in the array.

In the algorithm implementation, we ensure the regularization parameter λ for both schemes are adjusted appropriately so that the reconstructed results are optimized. For fair comparison, the phased array scheme adopts the same number of samples as the switched array scheme, which is 40% random measurements of the fully sampled switched array scheme. Fig. 6(a) and Fig. 6(b) demonstrate the CS reconstruction based on switched array scheme and phased array scheme, respectively, with 20 dB SNR. Both schemes show good agreement in reconstruction. However, when the SNR level is decreased to -50 dB, as shown in Fig. 6(c) and Fig. 6(d), the switched array scheme fails to reconstruct the targets as the background is filled with speckles. In contrast, the phased array scheme shows acceptable reconstruction with little background noise. More specifically, Fig. 7 depicts the averaged MSE of the two schemes as a function of SNR from -70 dB to 30 dB. For each SNR value, 10 independent trails are used to compare with the ground truth. It can be noticed that the phased array scheme achieves much lower MSE than the switched array scheme in the low SNR cases. However, this advantage gradually disappears as the SNR increases to 30 dB, which indicates both schemes, when combined with CS theory, have very similar performance when noise contribution is low.

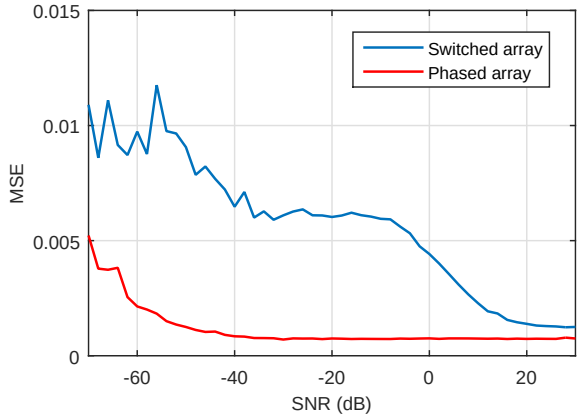

Fig. 7. Averaged MSE comparison of switched array and phased array schemes as a function of SNR.

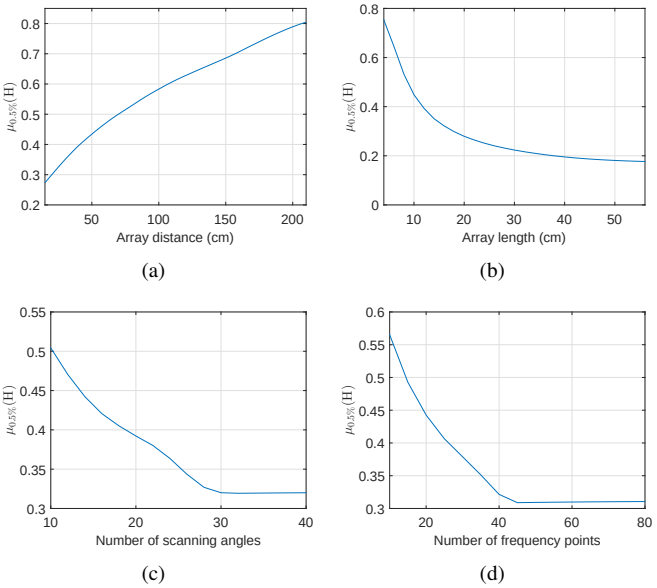

Fig. 8. The $t_{\%}$-average mutual coherence as a function of (a) array distance, (b) array length (c) number of angles and (d) number of frequency points.

C. Input Parameters and Coherence Analysis

As previously explained in section III, mutual coherence of the sensing matrix is proportional to the MSE values of reconstruction. In our phased array system, the sensing matrix is determined by many factors like array aperture, scanning region, frequency range and so on. With these parameters, we are more interested to design a sensing configuration such that high quality reconstruction can be achieved. Therefore, for each realization of $\mathbf{H}$, we measure its $t_{\%}$-average mutual coherence as a prediction of the reconstruction quality. The parameter t is set as 0.5, which is shown to better agrees with the MSE trend [22]. All simulations are based on the 2-D case for simplicity. Only one parameter is varied at a time and other parameters are kept fixed to avoid interference. The reconstruction region is fixed in a 30 cm$\times$30 cm area with a discretization of 101$\times$101 pixels.

We first vary the distance between the array aperture and the reconstruction region. Forty frequency points and 80 angles are adopted for illumination. The array aperture is of length 16 cm in cross-range dimension. Fig. 8(a) shows the $\mu_{0.5\%}(\mathbf{H})$ increases as the distance goes farther. This is expected because the distance difference among adjacent pixels approaches zero as the distance approaches infinite. In other words, the columns of $\mathbf{H}$ becomes less independent as the distance increases. Therefore, compressive phased array technique is better-behaved in the close range of the array aperture. It is worth noting that, according to the same mechanism, the high coherence can be avoided by moving the phased array to form a larger synthetic aperture.

The array length is another important factor in the phased array system. For an array of fixed element spacing, larger array means more elements. Increasing the number of elements further increases the directivity of the array, which results in more distinct system responses from pixels that are far apart from one another in cross-range direction. Fig. 8(b) clearly interprets this relationship when 40 frequency points and 100 angles are adopted for a reconstruction area from 35 cm to 65 cm. However, increasing the array size is less effective when the length is greater than 20 cm.

Unlike the array length which is usually fixed in a given system, the range of frequencies and scanning angles are more easily adjustable. Fig. 8(c) and Fig. 8(d) represent the $\mu_{0.5\%}(\mathbf{H})$ variation as a function of the number of angles and frequency points, respectively. Both curves show coherence reduction as the number increases. As previously shown in III, the number of rows of $\mathbf{H}$ is determined by the total number of frequency points and angles used. Increasing the number of frequency points or angles increases the dimension of the column vectors in $\mathbf{H}$. With fixed number of columns in $\mathbf{H}$, increased dimension provide more information and hence make the columns more unique from one another. Then, similar to the array length case, when the number is increased to a certain level, the $\mu_{0.5\%}(\mathbf{H})$ does not decrease anymore.

V. Conclusion

In this paper, a 3-D compressive imaging model has been derived for phased array systems. With the CS theory, far fewer angles and frequency points are required for image reconstruction, which further accelerate the scanning speed of phased array imaging systems. The image reconstruction performance of the proposed method are demonstrated both with qualitative and quantitative results. Particularly, the resolving power has been significantly enhanced about 74% and 68% in range and cross-range dimensions, respectively. The effect of implementation aspects including array distance, array length, number of angles and number of frequency points have also been presented as guidelines on how to design sensing configurations for better CS reconstruction. Future work will include techniques to reduce the computational complexity of the CS method.

References

[1] S. Kharkovsky and R. Zoughi, "Microwave and millimeter wave nondestructive testing and evaluation - overview and recent advances," *IEEE Instrumentation Measurement Magazine*, vol. 10, no. 2, pp. 26–38, April 2007.

[2] D. M. Sheen, D. L. McMakin, and T. E. Hall, "Three-dimensional millimeter-wave imaging for concealed weapon detection," *IEEE Transactions on Microwave Theory and Techniques*, vol. 49, no. 9, pp. 1581–1592, 2001.

[3] E. C. Fear, X. Li, S. C. Hagness, and M. A. Stuchly, "Confocal microwave imaging for breast cancer detection: localization of tumors in three dimensions," *IEEE Transactions on Biomedical Engineering*, vol. 49, no. 8, pp. 812–822, Aug 2002.

[4] A. Gonzalez-Ruiz and Y. Mostofi, "Cooperative robotic structure mapping using wireless measurements-a comparison of random and coordinated sampling patterns," *IEEE Sensors Journal*, vol. 13, no. 7, pp. 2571–2580, 2013.

[5] L. Zhang, Y. Hao, and C. Parini, "Millimetre wave imaging system parameters at 95 ghz," *Microwaves, Antennas Propagation, IET*, vol. 5, no. 5, pp. 528–534, April 2011.

[6] J. Li, P. Stoica, and X. Zheng, "Signal synthesis and receiver design for mimo radar imaging," *IEEE Transactions on Signal Processing*, vol. 56, no. 8, pp. 3959–3968, Aug 2008.

[7] X. Zhuge and A. G. Yarovoy, "Three-Dimensional Near-Field MIMO Array Imaging Using Range Migration Techniques," *IEEE Transactions on Image Processing*, vol. 21, no. 6, pp. 3026–3033, June 2012.

[8] E. Fishler, a. Haimovich, R. Blum, D. Chizhik, L. Cimini, and R. Valenzuela, "MIMO radar: an idea whose time has come," *Proceedings of the 2004 IEEE Radar Conference (IEEE Cat. No.04CH37509)*, pp. 71–78, 2004.

[9] S. S. Ahmed, A. Schiessl, and L. P. Schmidt, "A novel fully electronic active real-time imager based on a planar multistatic sparse array," *IEEE Transactions on Microwave Theory and Techniques*, vol. 59, no. 12, pp. 3567–3576, Dec 2011.

[10] M. Soumekh, "Array imaging with beam-steered data," *IEEE Transactions on Image Processing*, vol. 1, no. 3, pp. 379–390, Jul 1992.

[11] D. Donoho, "Compressed sensing," *Information Theory, IEEE Transactions on*, vol. 52, no. 4, pp. 1289–1306, April 2006.

[12] E. Candes, J. Romberg, and T. Tao, "Robust uncertainty principles: exact signal reconstruction from highly incomplete frequency information," *Information Theory, IEEE Transactions on*, vol. 52, no. 2, pp. 489–509, Feb 2006.

[13] C. F. Cull, D. A. Wikner, J. N. Mait, M. Mattheiss, and D. J. Brady, "Millimeter-wave compressive holography," *Appl. Opt.*, vol. 49, no. 19, pp. E67–E82, Jul 2010.

[14] L. Qiao, Y. Wang, Z. Shen, Z. Zhao, and Z. Chen, "Compressive sensing for direct millimeter-wave holographic imaging," *Appl. Opt.*, vol. 54, no. 11, pp. 3280–3289, Apr 2015.

[15] Q. Cheng, A. Alomainy, and Y. Hao, "On the performance of compressed sensing-based methods for millimeter-wave holographic imaging," *Appl. Opt.*, vol. 55, no. 4, pp. 728–738, Feb 2016.

[16] V. Patel, G. Easley, J. Healy, D.M., and R. Chellappa, "Compressed synthetic aperture radar," *Selected Topics in Signal Processing, IEEE Journal of*, vol. 4, no. 2, pp. 244–254, April 2010.

[17] J. Yang, J. Thompson, X. Huang, T. Jin, and Z. Zhou, "Random-frequency sar imaging based on compressed sensing," *Geoscience and Remote Sensing, IEEE Transactions on*, vol. 51, no. 2, pp. 983–994, 2013.

[18] W. Qiu, J. Zhou, H. Zhao, and Q. Fu, "Three-dimensional sparse turntable microwave imaging based on compressive sensing," *Geoscience and Remote Sensing Letters, IEEE*, vol. 12, no. 4, pp. 826–830, April 2015.

[19] H. Kajbaf, J. T. Case, Z. Yang, and Y. R. Zheng, "Compressed sensing for sar-based wideband three-dimensional microwave imaging system using non-uniform fast fourier transform," *IET Radar, Sonar & Navigation*, vol. 7, no. 6, pp. 658–670, 2013.

[20] L. Carin, D. Liu, W. Lin, and B. Guo, "Compressive sensing for multi-static scattering analysis," *Journal of Computational Physics*, vol. 228, no. 9, pp. 3464–3477, 2009.

[21] A. Massa, P. Rocca, and G. Oliveri, "Compressive sensing in electromagnetics - a review," *IEEE Antennas and Propagation Magazine*, vol. 57, no. 1, pp. 224–238, Feb 2015.

[22] I. Stojanovic, M. Cetin, and W. C. Karl, "Compressed sensing of monostatic and multistatic SAR," *IEEE Geoscience and Remote Sensing Letters*, vol. 10, no. 6, pp. 1444–1448, 2013.

[23] R. J. Mailloux, "Phased array antenna handbook," *Boston, MA: Artech House, 1994.*, 1994.

[24] S. Patole and M. Torlak, "Two dimensional array imaging with beam steered data," *IEEE Transactions on Image Processing*, vol. 22, no. 12, pp. 5181–5189, Dec 2013.

[25] S. S. Chen, D. L. Donoho, and M. A. Saunders, "Atomic decomposition by basis pursuit," *SIAM review*, vol. 43, no. 1, pp. 129–159, 2001.

[26] J. M. Bioucas-Dias and M. A. Figueiredo, "A new twist: two-step iterative shrinkage/thresholding algorithms for image restoration," *Image Processing, IEEE Transactions on*, vol. 16, no. 12, pp. 2992–3004, 2007.

[27] E. J. Cands, "The restricted isometry property and its implications for compressed sensing," *Comptes Rendus Mathematique*, vol. 346, no. 910, pp. 589 – 592, 2008.

[28] E. Candès and J. Romberg, "Sparsity and incoherence in compressive sampling," *Inverse Problems*, vol. 23, no. 3, pp. 969–985, 2007.

[29] J. M. Duarte-Carvajalino and G. Sapiro, "Learning to sense sparse signals: Simultaneous sensing matrix and sparsifying dictionary optimization," *IEEE Transactions on Image Processing*, vol. 18, no. 7, pp. 1395–1408, 2009.

[30] G. Lipworth, A. Mrozack, J. Hunt, D. L. Marks, T. Driscoll, D. Brady, and D. R. Smith, "Metamaterial apertures for coherent computational imaging on the physical layer," *J. Opt. Soc. Am. A*, vol. 30, no. 8, pp. 1603–1612, 2013.

[31] M. Elad, "Optimized projections for compressed sensing," *IEEE Transactions on Signal Processing*, vol. 55, no. 12, pp. 5695–5702, 2007.

[32] L. I. Rudin, S. Osher, and E. Fatemi, "Nonlinear total variation based noise removal algorithms," *Physica D: Nonlinear Phenomena*, vol. 60, no. 1, pp. 259–268, 1992.

[33] M. Soumekh. Phased array imaging of stationary targets. [Online]. Available: http://www.acsu.buffalo.edu/~msoum/